PREDICTION OF ENGINE INSTALLATION DRAG FOR THE DLR-F6 CONFIGURATION VIA CFD

Ricardo G. Silva, ri_galdino@yahoo.com.br[1]
João Luiz F. Azevedo, joaoluiz.azevedo@gmail.com[1]

[1]Instituto de Aeronáutica e Espaço, DCTA/IAE/ALA, São Josée dos Campos, SP, 12228-904, Brazil

Abstract: *Navier-Stokes simulations are performed to determine the engine installation drag. To this end, the DLR-F6 geometry, which has wind tunnel results and also numerical results available from the 2nd AIAA CFD Drag Prediction Workshop (DPW-II), is used. Moreover, these results are at hand for DLF-F6 configuration with and without pylon and nacelle. All the experimental results are acquired for a Mach number equal to 0.75 and a Reynolds number equal to 3 million. This test case is used as a part of an ongoing validation process of an in-house developed Computational Fluid Dynamics (CFD) code, denoted BRU3D, for aerospace applications. Three hybrid meshes with different refinement levels are generated in order to measure the mesh refinement effect on engine installation drag. In addition, at least three hexahedral (multiblock) meshes with different levels of refinement are also used to determine engine installation drag. These meshes are obtained from the DPW-II website. All the simulations are performed with the Spalart-Allmaras (SA) turbulence model. This paper present comparisons of drag polar with and without engines obtained from our numerical results and experimental results, in addition, the interference drag will be calculated at design point. Most of all results obtained so far show a satisfactory agreement with experimental results, the exceptions is the results obtained with hybrid coarse mesh for configurations with and without pylon and nacelle.*
Keywords: *Drag prediction, CFD, Engine installation drag, Turbulence modeling*

1. INTRODUCTION

High Reynolds number and also high Mach always occur in aerospace and aeronautics applications, such cases are the main focus of IAE (Instituto de Aeronáutica e Espaço). Once, a high Reynolds number is also typical conditions for IAE's cases an appropriated turbulence model must be available in the CFD solver (Computational Fluid Dynamics). In addition, this code should also be able to deal with flow features such as flow detachment, interaction between shock waves and boundary layer, confluence of boundary layer and flow wakes, etc., just to enumerated same that are more frequent on aerospaces and aeronautics flow.

The results that are presented in this article is focused on aeronautic application. Moreover, these results are part of an ongoing validation and improving the process of our in house CFD solver. This process is the way of achieving our final goal, which has a CFD solver that is capable to generate a realistic result in a robust way for a high number of different configurations. To be used as tool in the aircraft design, a CFD code should be able to capture, drag and lift generated for a given configuration. Another important feature is to be able to predict the variations on aerodynamic coefficients caused by a modification on geometries and also modification on the configurations. For instance, the CFD solver have shown the effects cause by the installation of underwing engines. This example has been the guideline of this paper, which means that our simulations are done with a configuration with engines (WBPN – Wing Body Pylon Nacelle) and, in order to verify the engine installation, a configuration without engines (WB – Wing Body).

For this investigation, the chosen test case is the DLR-F6, which are a public domain geometry and also was used at 2nd AIAA CFD Drag Prediction Workshop (DPW-II). In addition, there are a wind tunnel data available for flow conditions of Reynolds number equal to 3 million and Mach equal to 0.75 for both configurations with (WB) and without engine (WBPN). A drag polar for each model configuration (WB and WBPN) is calculated from the simulation results and compare to experimental data. Three different levels of mesh refinement for hybrid (prismatic + tetrahedral + pyramidal mesh element) and hexahedral mesh in conjugation with SA (Spalart-Allmaras) turbulence mode are used to generate the numerical results.

Unfortunately, we could not finish all simulations until now, the drag polar for some refinements level not have all points. However, for the final paper all the simulations will available. Those points that are missing do not have any important impact on the final conclusions.

2. CONFIGURATION and WIND TUNNEL TEST CONDITIONS

The test configuration DLR-F6 derives from DLR-F4, which was used in the DPW-I. Cruise condition of Mach number equal to 0.75 and lift coefficient equal to 0.50 was used as the design point for DLR-F6. The aspect ratio is equal to 9.5 and sweep angle equal to 27.1 degrees. Figure 1(a) shows the DLR-F6 plan view (O. Brodersen, 2001) of WBPN configurations.

The experimental data are available for both configurations with and without engines at the DPW-II web site (DWP-II, 2003). The engine installation effects are represented by a flow through nacelle. Figure 1(b) presents the model inside the wind tunnel. The nacelle exit is designed in order ensure that the mass flow rate is similar to the engine at cruise

conditions. Moreover, this modification on the nacelle exit, make sure that the nacelle stagnation line is in the same position as observed at the engine nacelle at cruise condition. Thus, the flow around and upstream the nacelle is similar to flow at this region during flight with operating engines.

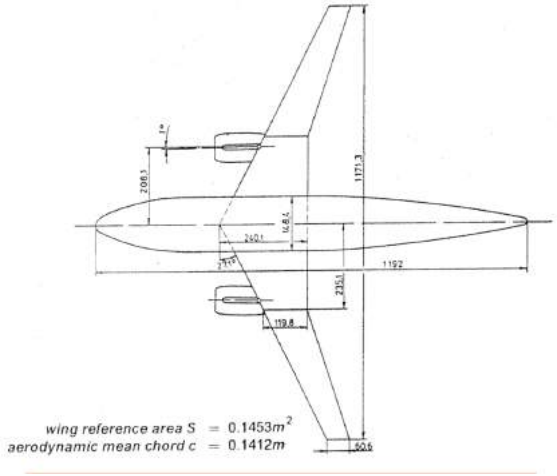

(a) DLR-F6 plane view

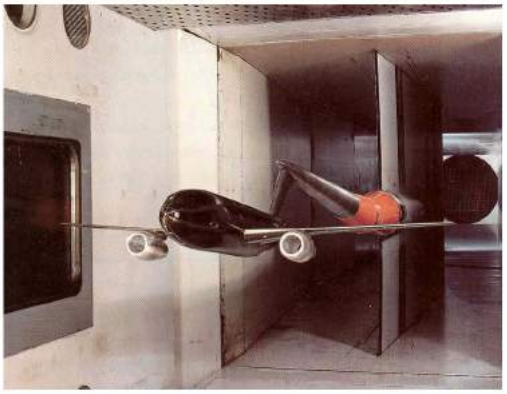

(b) DLR-F6 model inside the wind tunnel test section

Figure 1: **The DLR-F6 plane view quoted in mm, this figure was extracted from O. Brodersen (2001), and model inside the wind tunnel test section, with was extracted from DPW-II web site (DWP-II, 2003). The plane view was extracted from and**

The drag polar wind tunnel available at the DPWII web site (DWP-II, 2003) was obtained from an experimental test conducted at Reynolds number equal to 3 million and Mach number equal to 0.75. The numerical drag polar is obtained at the same condition of the wind tunnel test, for these simulations the Angle of Attack (AOA) equal to -3,-2,-1.5, 1, 0, 1 and 1.5 degree. These simulations were requested as one of the required cases for who was presenting the results to the workshop.

3. CONFIGURATION AND WIND TUNNEL TEST CONDITIONS

The numerical solutions are obtained with IAE CFD solver BRU3D, which is still under development. In which, the Reynolds-averaged Navier-Sokes equations are numerically solved. Moreover, BRU3D is cell-centred finite volume solver and is also cable to deal with a different element type, such as tetrahedral cells, prismatic cell, pyramidal cell and hexahedral cells.

In the section a brief description of a theoretical and numerical formulation implemented in BRU3D will be given. This section is mainly based on Bigarella and Azevedo (2009). The flows considered in the present paper are described by the 3-D compressible Reynolds averaged Navier-Stokes (RANS) equations and it is assumed to be fully turbulent. These equations in its dimensions form, are given by:

$$\frac{\partial Q}{\partial t} + \nabla \cdot (E_e - E_\nu) = 0 \tag{1}$$

on which Q is given by

$$Q = [\rho\ \rho u\ \rho v\ \rho w\ \rho\tau_1\ \rho\tau_2\ ]^T \tag{2}$$

and the inviscid (E_e) and viscous (E_ν) flux vectors are given by

$$E_e = \begin{Bmatrix} \rho\mathbf{v} \\ \rho u\mathbf{v} + p\widehat{i}_x \\ \rho v\mathbf{v} + p\widehat{i}_y \\ \rho w\mathbf{v} + p\widehat{i}_z \\ (e+p)\mathbf{v} \\ \tau_1\mathbf{v} \\ \tau 2\mathbf{v} \end{Bmatrix} \qquad E_\nu = \begin{Bmatrix} 0 \\ \left(\tau^l_{xj} + \tau^t_{xj}\right)\widehat{i}_j \\ \left(\tau^l_{yj} + \tau^t_{yj}\right)\widehat{i}_j \\ \left(\tau^l_{zj} + \tau^t_{zj}\right)\widehat{i}_j \\ \beta_j\widehat{i}_j \\ \mu_{diff_1}\tau_{1,j}\widehat{i}_j \\ \mu_{diff_2}\tau_{2,j}\widehat{i}_j \end{Bmatrix} \tag{3}$$

The shear-stress tensor is defined as

$$\tau^l_{ij} = \mu_l \left(\frac{\partial u_i}{\partial x_j} + \frac{\partial u_j}{\partial x_i} - \frac{2}{3}\frac{\partial u_m}{\partial x_m}\delta_{ij} \right) \tag{4}$$

on which u_I is velocity component, and x_I is referent to coordinate the system. The dynamic viscosity μ_l is determined by Sutherland law.

The unknown Favre averaged Reynolds stress tensor, τ^t , is modelled within BRU3D via linear Eddy-Viscosity Models (EVM). The linear EVM options used in the present paper are SA turbulence model shown at Spalart and Allmaras (1994).

The RANS equations (Eq. 1) and the turbulence model equations according to finite volume method are given by

$$V_i \frac{\partial Q_i}{\partial t} = -\sum_{k=1}^{nf} \left(E_{e_k} - E_{\nu_k}\right) \cdot S_k = -RHS \tag{5}$$

on which the subscript k stands for properties computed in the k^{th} face, and nf represents the number of faces, which form the i^{th} control volume. To obtain Eq. 5, it is assumed constant fluxes through volumes faces and also constant Q_i proprieties inside the volume faces. The first assumption is a sufficient approximation to obtaining $2nd$ order accuracy in space the currently available flux computation schemes. In the convective flux computation, a Roe flux-difference splitting scheme (Roe, 1981) is assumed. To achieve 2^{nd} order accuracy in space, primitive properties are linearly reconstructed at volume faces with MUSCL algorithm (van Leer, 1979) in conjugation with limiter function, such as minmod, van Albada or super bee limiters (Hirsh, 1991) that are currently available in BRU3D. The present effort uses van Albada as limiter function. The diffusion terms are discretized using a method that computes a non oscillation, highly accurate derivatives at the face, as described in Bigarella (2007).

A $1st$ order backward Euler implicit non-linear scheme for Eq. 5 is given by

$$V_i \frac{\Delta Q_i^n}{\Delta t} = -RHS\left(Q_i^{n+1}\right) \tag{6}$$

Here, $\Delta Q_i^n = Q_i^{n+1} - Q_i^n$. The linearisation use an expansion of $RHS\left(Q_i^{n+1}\right)$ about ΔQ_i^n as in

$$RHS\left(Q_i^{n+1}\right) = RHS\left(Q_i^n\right) + \frac{\partial RHS\left(Q_i^n\right)}{\partial Q_i^n} \Delta Q_i^n + O\left(\Delta Q_i^n\right)^2 \tag{7}$$

and leads to the 1^st order accurate implicit scheme:

$$V_i \frac{\Delta Q_i^n}{\Delta t} + \frac{\partial RHS\left(Q_i^n\right)}{\partial Q_i^n} \Delta Q_i^n = -RHS\left(Q_i^n\right) \tag{8}$$

More detail on how to calculate the residue $\left(RHS\left(Q_i^n\right)\right)$, the Jacobian $\left[\frac{\partial RHS(Q_i^n)}{\partial Q_i^n}\right]$, and flux can be found in Bigarella and Azevedo (2009).

4. MESH

The numerical simulations will emulate a free fight condition. Hence, it is not necessary to include the wind tunnel walls in the numerical domain. However, all the experimental data were acquired from wind tunnel runs that always present wall effect. To eliminate these effects a correct methodology had been applied to the experimental data. Therefore, all the comparisons, which are going to be presented in section 5. between experimental data and numerical results were done within compatible conditions. All the experimental results available at DPW-II web site (DWP-II, 2003) represent free fight, which means that all date received the appropriated corrections.

The numerical domain consists of a semi-sphere placed at a distance equal to two hundred Mean Aerodynamic Chord (MAC) from the DLF-F6 wing surface, this quit a large distance is used to try to avoid any effect of boundary conditions on the near field flow solution. The semi-spherical outside part of the numeric domain is called Far Field and the characteristic equations imposed as a boundary condition. Moreover, a no slip condition imposed to the wing surface. This description is valid just for hybrid meshes, once these were generated by the authors. The hexahedral mesh was taken from DPW-II web site (DWP-II, 2003) and the far field seems to be even more distant than 100 times the MAC. However, the far field has a rectangular shape.

Both meshes hybrid and hexahidral are divided in three levels of refinement. The generation mesh process is reported just for the hybrid meshes and we limit ourselves just to make analyses above hexahidral meshes by comparing those between them and by comparison with hybrid meshes. More details on hexahidral meshes can be found at DPW-II web site (DWP-II, 2003). It worth to mention that the mesh refinement level is classified as fine, medium and coarse, whereas in our case we just change the nomenclature from medium to baseline. Thus, the meshes in the present study are classified as fine, baseline and coarse.

To generate a sequence of meshes with different levels of refinement, we use factor for the surface element size and for the element number inside the prismatic layer. The number of elements inside the boundary layer is multiplied by two and the size of a surface element, which represent the surface refinement, is divided by two from one refinement level to the less refinement level. The hybrid meshes are composed of prismatic, pyramidal and tetrahedral elements. The elements attached to the wing wall surface have their Y^+ equal to 1, which means that all meshes give support to solve the boundary layer without any approximation.

Figure 2 shows all hybrid surface mesh that is generated to evaluate the mesh effect on the engine installation drag. Our process of mesh generations starts from the fine mesh of WBPN configuration and a factor of two, as described before, is applied once to obtain the baseline mesh and twice to obtain the coarse mesh. In order to maintain the same mesh surface refinement between WBPN and WB meshes, each level of surface mesh refinement of WBPN configuration is used to generate its respective WB surface mesh. It is achieved by removing the pylon and nacelle surface mesh, this process leaves a hole at lower surface located where the plane was fixed. At the end, this hole is closed and the WB surface mesh is obtained.

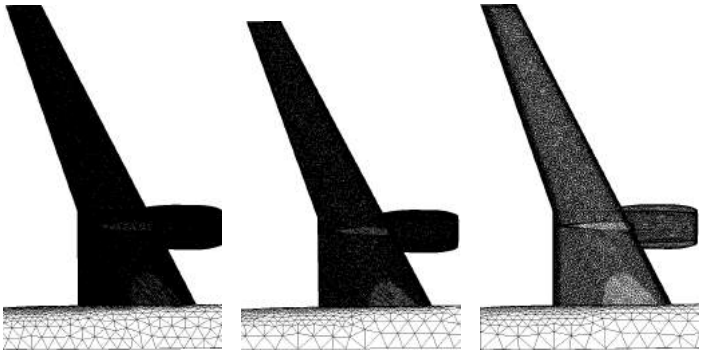

(a) WBPN-Fine Mesh (b) WBPN-Baseline Mesh (c) WBPN-Coarse Mesh

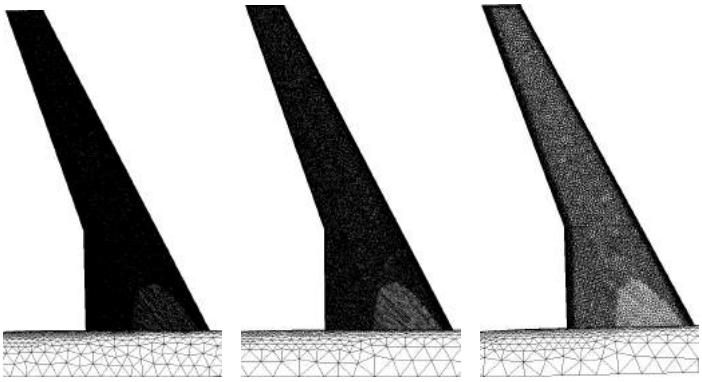

(d) WBPN-Fine Mesh (e) WBPN-Baseline Mesh (f) WBPN-Coarse Mesh

Figure 2: **Three level of hybrid surface mesh for WBPN and WB configuation.**

The trailing edge and wing tip has different levels of refinement when it is compared with the rest of the wing surface. At the trailing edge, this refinement is not only because of the surface curvature, but also, because it is expected a high variation of the pressure.

Close to the wing tip the volumetric mesh refinement is mainly improved by adding by selecting a region around the wing tip, inside this region the element size is fixed, in our case this volumetric element size is equal to its respective surface element size. This approach is used to try to improve the resolution of wing tip vortex. A similar approach is used in regions near to the wing trailing edge and wing leading edge.

The hexahedral surface meshes are presented in Fig. 3 for WBPN configuration and WB configuration. It is possible to realize that mesh surfaces from each level of refinement are similar. Moreover, it is noticeable that the refinement factor is less than 2.

Figures 4 and 5 highlights the difference on the volumetric mesh due to the refinement process. The tetrahedral growth ratio is the same for all three meshes, consequently all the volumetric refinement is directly related to the surface mesh refinement. On the other hand, not is the prismatic layer height ratio identical for all meshes, once we use the number of elements inside of the prismatic layer as a control parameter for mesh refinement. As a consequence, this definition, the coarse mesh seems to not have enough refinement in prismatic layer, which is direct linked to the level of resolution of the boundary layer. Thus, it is expected a result somewhat worse for coarse hybrid mesh than the results for the other meshes. Despite the fact with the coarse prismatic layer, all the volumetric meshes seem to have a smooth growth of its volumetric elements.

5. RESULTS

All the calculations have been performed at Reynolds number equal to 3.10^6 and Mach number equal to 0.75. The turbulence model SA available in BRU3D does not have a capability to predict the boundary layer transition, thus all simulations are full turbulent. Moreover, the CFL is equal to 10 and the number of solver iterations is limited to 3000, and after a 1500 iteration the van Albada limiter is frozen. For instance, Fig. 6 shows the convergence history of continuity equation, CL (lift coefficient) and CD (drag coefficient) for WBPN configuration hexahedral coarse mesh. The effect of

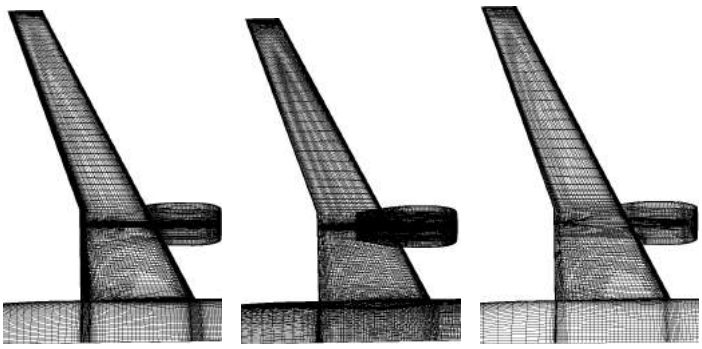

(a) WBPN-Fine Mesh (b) WBPN-Baseline Mesh (c) WBPN-Coarse Mesh

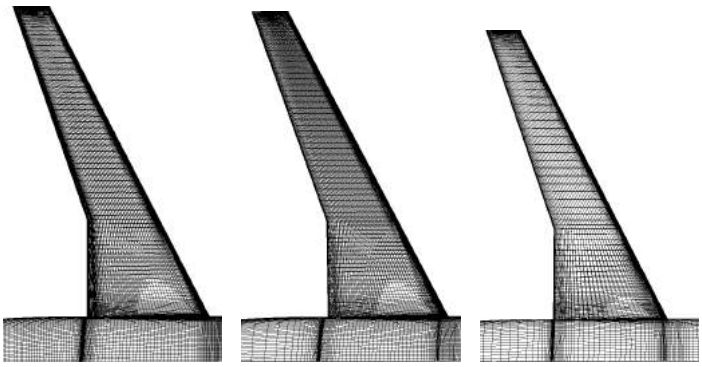

(d) WB-Fine Mesh (e) WB-Baseline Mesh (f) WB-Coarse Mesh

Figure 3: **Three level of hexahedral surface mesh for WBPN and WB configuation.**

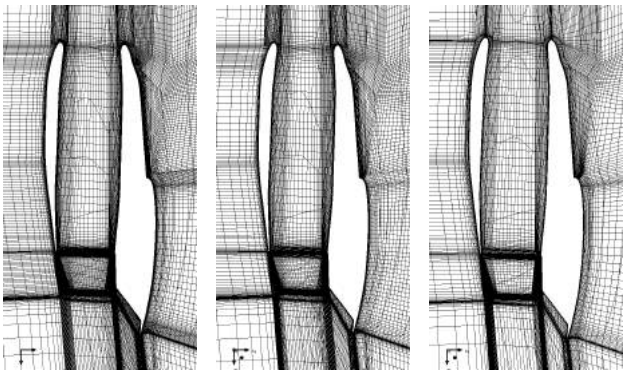

(a) WBPN-Fine Hexahedral Mesh. (b) WBPN-Baseline Hexahedral Mesh. (c) WBPN-Coarse Hexahedral Mesh.

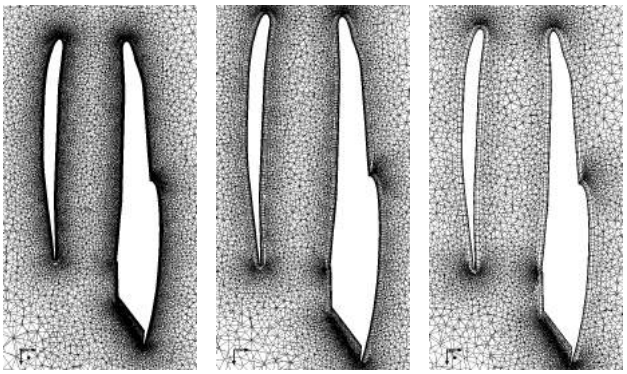

(d) WBPN-Fine Hybrid Mesh. (e) WBPN-Baseline Hybrid Mesh. (f) WBPN-Coarse Hybrid Mesh.

Figure 4: **Three level of hexahedral surface mesh for WBPN and WB configuation.**

frozen the limiter is exhibited in Fig. 6(a), it is possible to visualize that the continual equation residual stalls after 400 iterations and it remains flapping between -2 and -3 until the moment when the limiter is frozen. After that point the residual starts to fall again and it stays falling up to the maximum number of iterations. In addition, the CL and CD seem

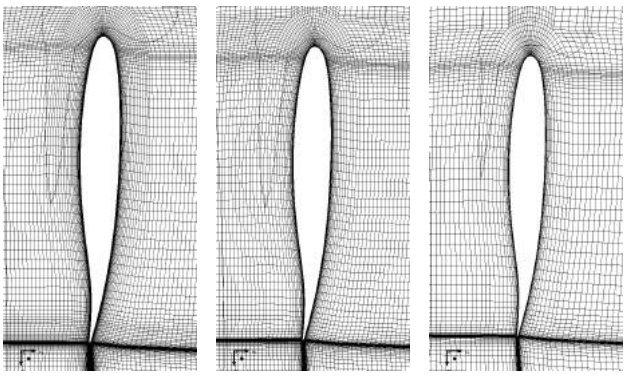

(a) WB-Fine Hexahedral Mesh. (b) WB-Baseline Hexahedral Mesh. (c) WB-Coarse Hexahedral Mesh.

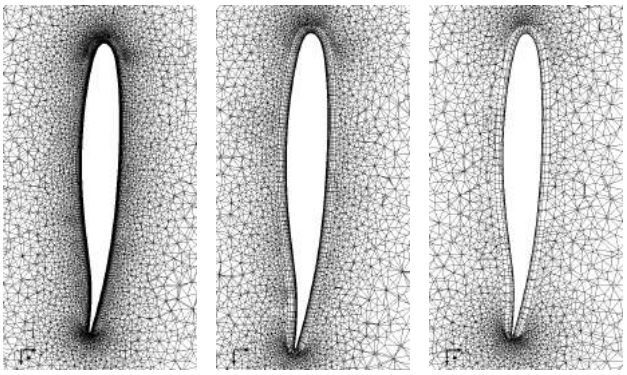

(d) WB-Fine Hybrid Mesh. (e) WB-Baseline Hybrid Mesh. (f) WB-Coarse Hybrid Mesh.

Figure 5: **Three level of hexahedral surface mesh for WBPN and WB configuation.**

to converge after a 1000 iterations. All others simulations have similar behaviour continuity residual convergence history, CL convergence history and CD convergence history.

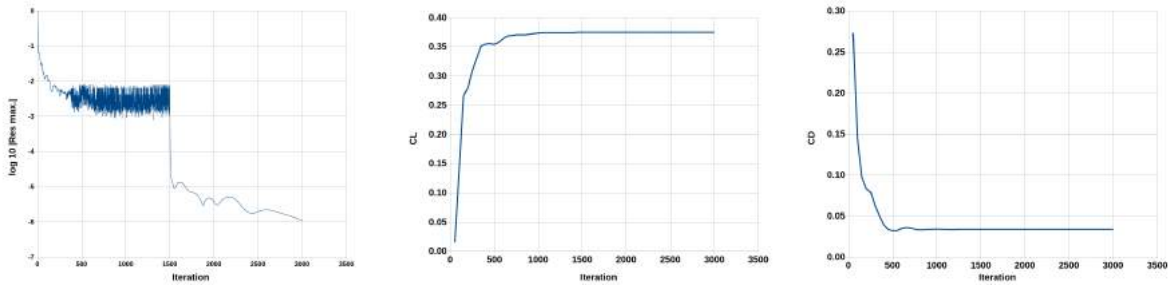

(a) Convergence history of continuity equation. (b) Convergence history of CL. (c) Convergence history of CD.

Figure 6: **The convergence history of continuity equation, CL (lift coefficient) and CD (drag coefficient) for numerical simulation of WBPN configuration hexahedral mesh.**

Figure 7 presents examples of Cp (pressure coefficient) over upper and lower wing surface of configuration WB and WBPN at AOA equal to 0 degree. By means of comparison between the WB Cp distribution and WBPN Cp distribution, a qualitative analysis of the effect of the pylon and nacelle installation is possible. From that comparison, it is noticeable the effect of the pylon and nacelle on the wing upper surface. Figure 7(a) shows a the inboard part. On the other hand, it is not so clear the effect on the wing lower surface of this qualitative analysis. Figure 7(a) shows that for WB configuration the negative peaks of CP are distributed over the wing span, however for WBPN configuration (Fig. 7(c)) the Cp negative peaks are limited to the inboard part of the wing.

Figure 8 presents the comparison of the computed drag polar and lift curve for the all three refinements levels of hexahedral mesh with experimental. It added and subtracted 50 drag counts from experimental drag values in order to stipulate a range of variation, in which all numerical results should be inside. These upper and lower limits will be shown in all drag polars that are the presented in present study. The comparison between experimental and numerical drag polar shown in Fig. 8(a) s revels a good agreement for all mesh refinement levels, since most of all points are inside the stipulated range of variation.

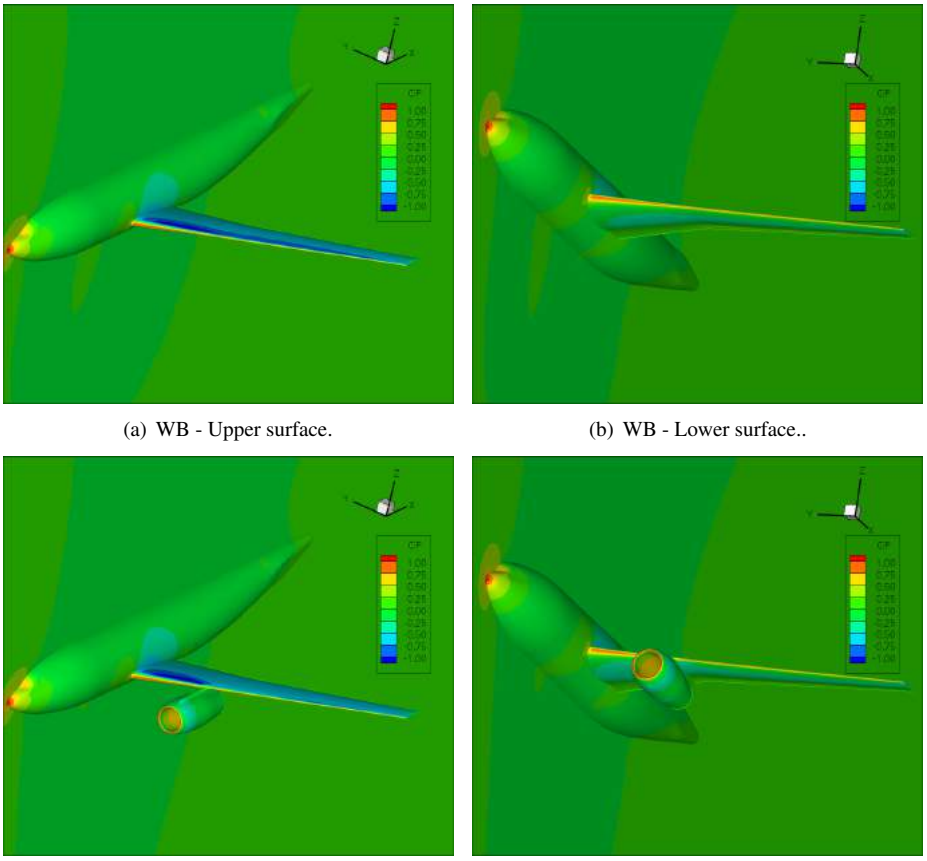

(a) WB - Upper surface. (b) WB - Lower surface..

(c) WBPN - Upper surface.. (d) WBPN - Lower surface..

Figure 7: **Pressure coefficient (Cp) distribution over a DLR-F6 with and without pylon and nacelle. The solutions presented in this figure was obtained with hexahedral coarse mesh at Reynolds number equal to 3.10^6, Mach number equal to 0.75 and AOA equal to 0 degree**

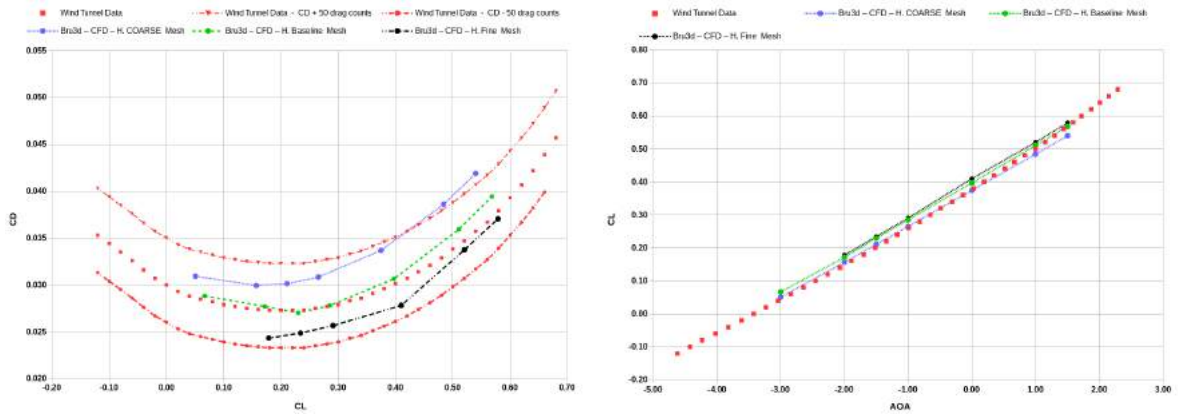

(a) WBPN Drag Polar (b) WBPN Lift Curve

Figure 8: **Comparison between experimental and numerical results for DLR-F6 WBPN configuration at Reynolds number equal to 3.10^6 and Mach number equal to 0.75. The drag polar and lift curve were obtained with BRU3D using the hexahidral mesh. The abbreviation H. in the legends stands for hexahidral.**

Figure 9 shows the polar drag and the lift curve obtained from a WB configuration with hexahedrica mesh. All drag polars obtained so far from that configuration falls within the range of variation of ± 50 counts drag (Fig. 9(a)) from the experimental polar drag. The CL results, which are presented in Fig. 9(b), for that configuration has error related to experimental results less than 3%.

The coarse hybrid mesh of both WBPN configuration and WB configuration present the worse the results. All results fall outside of the drag polar range, which can be seen in Figs. 10(a) for WBPN configuration and 11(a) for WB configuration. The results that were obtained with other mesh refinement levels (baseline mesh and fine mesh) fall within the variation range assumed for experimental drag polar. The results of WBPN configuration with hybrid fine mesh are the best of all simulations performed for DLR-F6 geometry, since the numerical results are very close to the results obtained

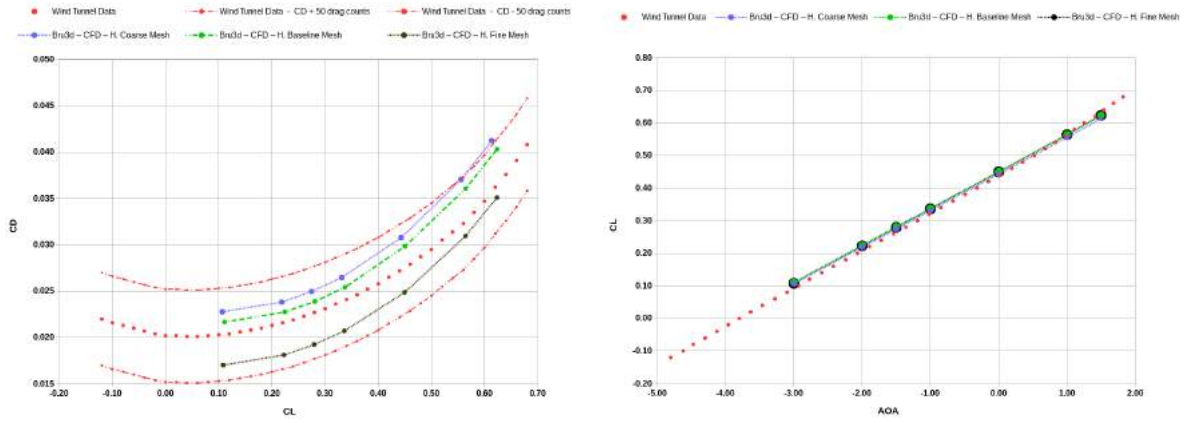

(a) WB Drag Polar (b) WB Lift Curve

Figure 9: **Comparison between experimental and numerical results for DLR-F6 WB configuration at Reynolds number equal to 3.10^6 and Mach number equal to 0.75. The drag polar and lift curve were obtained with BRU3D using the hexahidral mesh. The abbreviation H. in the legends stands for hexahidral.**

from the wind tunnel test, Fig. 10(a) shows the plot used to verify the proximity between numerical results and experimental results. However, this behaviour was not observed for WB configuration (Fig. 11(a)). The CD final results for this case is higher than the wind tunnel values, the main reason for this fact is related to differences in the Roe's numerical dissipation value, which was modified in order to maintain numerical solution stable. Yet further studies are necessary to confirm this relation.

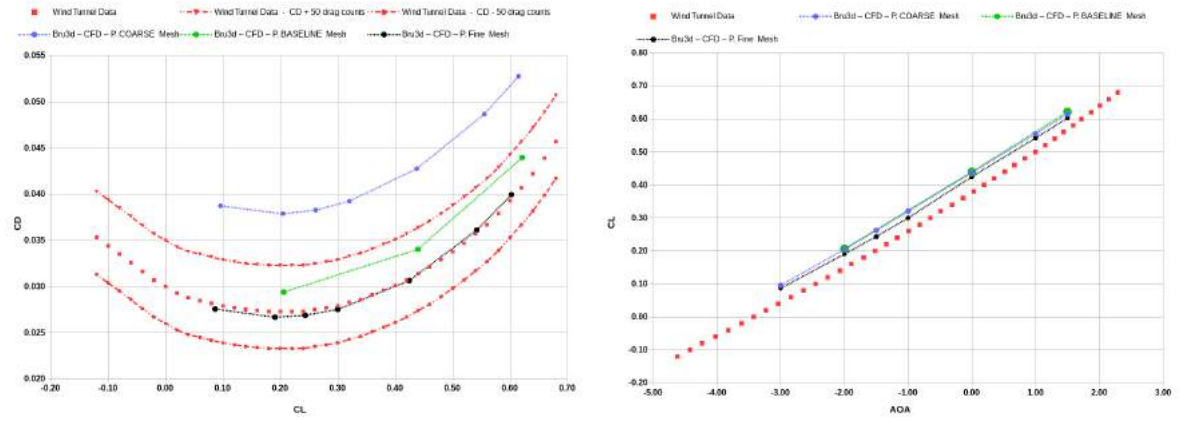

(a) WBPN Drag Polar (b) WBPN Lift Curve

Figure 10: **Comparison between experimental and numerical results for DLR-F6 WBPN configuration at Reynolds number equal to 3.10^6 and Mach number equal to 0.75. The drag polar and lift curve were obtained with BRU3D using the hybrid mesh. The abbreviation P. in the legends stands for prismatic and it refers to a hybrid mesh.**

The prediction of the engine installation drag is given by:

$$CD_I = CD_{WBPN} - CD_{WB} - CD_{Internal} \tag{9}$$

in which CD_I stands for the engine installation drag coefficient, CD_{WBPN} is the drag coefficient of WBPN configuration, CD_{WB} is the drag coefficient of WB configuration and $CD_{Internal}$ takes into account the drag coefficient of nacelle's internal parts. The DLR-F6 has its engines represented as flow through nacelle, which means that nacelle has internal part which produces drag. However, to define which part of the nacelle is internal or external, it is necessary to know the stagnation line position at the nacelle lip in order to separate the inner part ant outer part. In addition, the stagnation line position varies with AOA variations, which make these calculations a difficult task even for CFD, once it is needed not only a different mesh for each AOA in order to separate the nacelle in its outer and inner part, but also two simulations for each AOA, since it's necessary to define the stagnation line position before the process of mesh generation. In the tunnel the measure of nacelle internal drag is performed in a simplified manner (considering the stagnation line only for one AOA) with isolated nacelle. The same procedure could be done with CFD. For a real aircraft project this drag must be calculated and deducted from the total drag, since this drag was introduced in the process of engines simplification for to the wind tunnel test. In the present effort the nacelle internal drag is part of engine installation drag,

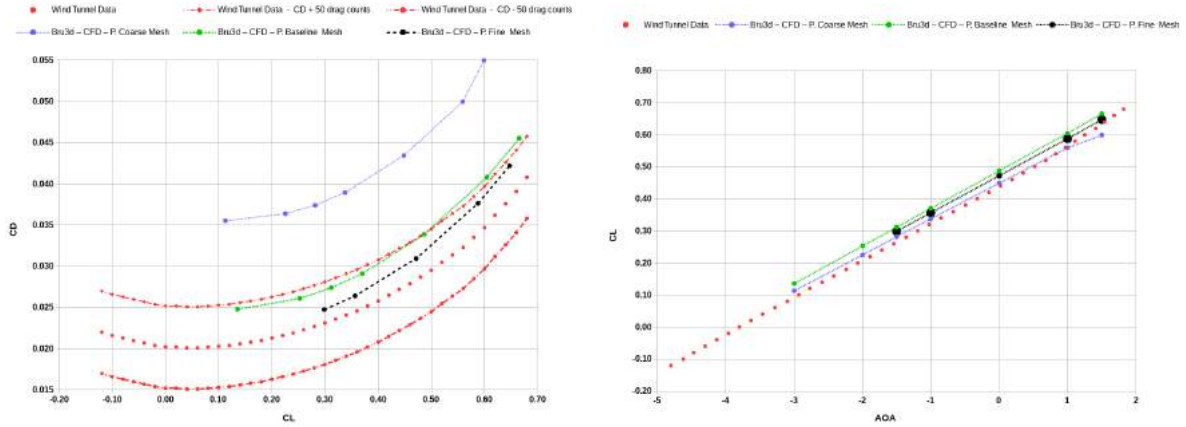

(a) WB Drag Polar

(b) WB Lift Curve

Figure 11: **Comparison between experimental and numerical results for DLR-F6 WB configuration at Reynolds number equal to 3.10^6 and Mach number equal to 0.75. The drag polar and lift curve were obtained with BRU3D using the hybrid mesh. The abbreviation P. in the legends stands for prismatic and it refers to a hybrid mesh.**

because of this the Eq. 10 is simplified and is given by:

$$CD_I = CD_{WBPN} - CD_{WB} \tag{10}$$

Tabela 1: **Engine interference drag at CL = 0.5**

	CD_{WBPN}(drag count)	CD_{WB}(drag count)	CD_i	$Error = 100\frac{CD_{I\_CFD} - CD_{I_{WT}}}{CD_{I\_WT}}$
CFD - Hybrid Coarse Mesh	458.9	464.9	-6.0	113.84%
CFD - Hybrid Baseline Mesh	373.3	346.5	26.7	37.84%
CFD - Hybrid Fine Mesh	341.5	325.9	15.6	63.70%
CFD - Hexahedral Coarse Mesh	395.4	330.2	65.2	51.59%
CFD - Hexahedral Baseline Mesh	354.5	325.6	28.9	32.71%
CFD - Hexahedral Fine Mesh	326.6	275.4	51.2	19.06%
Wind Tunnel	338	295	43	0%

Table 5presents the results for installation drag (CD_i) at CL equal to 0.5, which is the lift coefficient used at DLR-F6 design point. Those results were calculated from the results obtained from all meshes and also from a wind tunnel test. The relative error between the experimental results and numerical results decreases when the mesh refinement increases. This true for Hexahedral meshes and for Hybrid meshes, with the exemption of hybrid fine mesh result. This different behaviour is related to level of numerical dissipation introduces in the Roe method, which is not the same for WBPN and WB. The relative error has value that can be considered too high to be used in aircraft design process, if just the absolute CD value for installation drag is important. From our interpretation, this is just a clear indication that we need to increase the mesh refinement level, in other words, our fine mesh is not fine enough. However, all the results presented shows that the numerical methodology used in the present study is able to capture the engine installations drag.

6. CONCLUSION

The engine installation changes significantly the pressure distribution over the wing upper surface for AOA equal to 0 degrees. A local modification on the wing-pylon junction could improve the pressure distribution, however, it could be a solution that is valid just for this specific flow condition. This effect can only be really dished, if the wing design were done with the presence of engine in the model geometry consider for wing design.

The worse drag polar prediction was obtained for hybrid coarse mesh. This result is probably linked to the fact that these meshes do not have enough refinement on the boundary layer region (Figs. 4(f) and 5(f)). The results with baseline hybrid mesh and fine hybrid mesh present an improvement on the drag polar prediction. That improvement is directed related to the increase of mesh refinement, which not only increases the number of elements inside the boundary layer, but also increases the surface refinement. However, to define which of them and more significant, it is necessarily more specific studies.

Most of results obtained with the hexahedral mesh fall inside the assumed drag polar range (± 50 around the experimental drag polar). The only exception is the result for AOA equal to 1.5 degrees, this occurs for WBPN and WB configuration.

All the results presented shows that the numerical methodology used in the present study is able to capture the engine installations drag.

7. ACKNOWLEDGEMENTS

The authors gratefully acknowledge the support for the present research provided by Conselho Nacional de Desenvolvimento Científico e Tecnológico, CNPq, under the Research Grants No. 309985/2013-7, No. 400844/2014-1 and No. 443839/2014-0. The work is also supported by Fundação de Amparo à Pesquisa do Estado de São Paulo, FAPESP, under Research Grant No. 2013/07375-0.

8. REFERENCES

Bigarella, E. and Azevedo, J.L.F., 2009. "A unified implicit cfd approach for turbulent-flow aerospace-configuration simulations". In *Proceedings of the 47th AIAA Aerospace Sciences Meeting Including The New Horizons and Aerospace Exposition*. Orlando, USA.

Bigarella, E.D.V., 2007. *Advanced Turbulence Modelling for Complex Aerospace Applications*. Ph.D. thesis, Instituto Tecnolóco de Aeronáutica, Brazil.

Bordalo, S.N., Ferziger, J.H. and Kline, S.J., 1989. "The development of zonal models for turbulence". In *Proceedings of the 10th Brazilian Congress of Mechanical Engineering*. ABCM, Rio de Janeiro, Brazil, Vol. 1, pp. 41–44.

Clark, J.A., 1986. Private communication, University of Michigan, Ann Harbor.

Coimbra, A.L., 1978. *Lessons of Continuum Mechanics*. Ed. Edgard Blücher, São Paulo, Brazil. 428 p.

DWP-II, 2003. "2nd drag predction worshop". URL `http://aiaa-dpw.larc.nasa.gov/Workshop2/workshop2.html`. Accessed April 10, 2016.

Hirsh, C., 1991. *Numerical Computational of Internal and External Flows*, Vol. 2. Wiley, Chichester, 1st edition.

O. Brodersen, A.S., 2001. "Drag predction of engine-airframe interference effects using unstructured navier-stokes calculations". In *Proceedings of the 19th Appleid Aerodynamics Coference*. Anaheim, California.

Roe, P.L., 1981. "Approximate riemmann solvers, parametes vectos, and difference schemes". *Journal of Computational Physics*, Vol. 43, No. 2, pp. 357–372.

Spalart, P.R. and Allmaras, S., 1994. "A one-equation turbulence model for aerodynamic flow". *La Recherche Aeropastiale*, Vol. 1, pp. 5–21.

Sparrow, E.M., 1980. "Forced convection heat transfer in a duct having spanwise-periodic rectangular protuberances". *Numerical Heat Transfer*, Vol. 3, pp. 149–167.

van Leer, B., 1979. "Towards the ultimate conservative difference scheme. v. a second-order sequel to godunov???s method". *Journal of Computational Physics*, Vol. 32, No. 2, pp. 101–136.

9. RESPONSIBILITY NOTICE

The authors are solely responsible for the printed material included in this paper.